Electronic Supplementary Material (ESI) for Journal of Materials Chemistry A.

Supporting Information: Phase formation through synthetic control: polymorphism in the sodium-ion solid electrolyte $Na_4P_2S_6$

Tanja Scholz,[†,¶] Christian Schneider,[†,¶] Roland Eger,[†] Viola Duppel,[†] Igor Moudrakovski,[†] Armin Schulz,[†] Jürgen Nuss,[†] and Bettina V. Lotsch[*,‡,†]

†*Max Planck Institute for Solid State Research, Heisenbergstraße 1, 70569 Stuttgart, Germany*

‡*LMU Munich, Butenandstraße 5-13, 81377 Munich, Germany*

¶*Contributed equally to this work.*

E-mail: b.lotsch@fkf.mpg.de

Experimental Section

Syntheses

$Na_4P_2S_6$ was prepared using different synthesis routes:

The *solid-state reaction* was conducted according to Ref.[S1] . Stoichiometric amounts of Na (Alfa Aesar, 99.8%), P_4S_{10} (Acros, 98+%), and sulphur (Alfa Aesar, 99.5%, sublimed) were vacuum-sealed in double-walled silica tubes and heated slowly to the reaction temperature of 850 °C with $20\,\mathrm{K\,h^{-1}}$. This synthesis yields a highly crystalline white powder from which also colorless single crystals can be extracted.

Further, $Na_4P_2S_6$ was prepared *via* the *precipitation* of the hydrated compound $Na_4P_2S_6 \cdot 6\,H_2O$ and subsequent dehydration as in Ref.[S2] . $Na_2S \cdot 9\,H_2O$ (75 g; Aldrich, ≥99.99%) was dissolved in deionized water (100 ml) under stirring. Next, PCl_3 (6.6 ml; Arcos, 99%) was added slowly over 30 min due to its violent reaction with water. Then, the reaction vessel was placed in an ice bath, and the reaction was stirred for 20 min. During that time, white $Na_4P_2S_6 \cdot 6\,H_2O$ precipitated. The vessel was removed from the ice bath and stirred at room temperature for 1 h. Finally, the reaction mixture was stored at 4 °C over night. After that time, the crude reaction product was separated from the supernatant solution and recrystallized from an 80 °C water : ethanol solution (75:25). The dehydrated phase, $Na_4P_2S_6$, was obtained by heating the colorless crystals of the hexahydrate at 100 °C under dynamic vacuum for 12 h (Büchi furnace). The obtained powder is white and is characterized by inter- and intralayer defects.

On the cost of forming some side phases (e.g. phosphates), the precipitated $Na_4P_2S_6$ can be *annealed* to a product with less defects at 500 °C for 1 h in vacuum-sealed silica tube.

Powder X-Ray Diffraction

Powder X-Ray Diffraction (PXRD) patterns were measured using a STOE StadiP diffractometer (Mo $K\alpha_1$ radiation $\lambda = 0.7093\,\text{Å}$, curved germanium (111) monochromator, DECTRIS Mythen2R 1K detector) in Debye-Scherrer geometry. For room-temperature and high-temperature measurements, finely powdered samples were filled in capillaries of 0.3 mm and 0.5 mm diameter borosilicate and quartz glass (HILGENBERG), respectively. The capillaries were sealed under argon. High-temperature patterns were collected using a STOE capillary furnace. Data collection was done in the range from 2° to 50° 2θ with a step size of 0.015° for temperatures from 20 °C to 300 °C in steps of 10 °C or 20 °C. All data analysis was performed with JANA2006.[S3] The structure of β-$Na_4P_2S_6$ was solved starting from the α structure and evaluating the residual electron density at the $2d$ position. For the Rietveld refinements[S4] a pseudo-Voigt function with axial divergence was utilized. The sum of occupation of Na2 and Na3 were constrained to one to comply with the chemical formula. Errors of the results of the Rietveld refinements are specified as 3σ taking local correlations into account. To account for the higher sensitivity of the ${P_2S_6}^{4-}$ tilting, uncertainties were adjusted upwards for internal consistency. Detailed data of the temperature-dependent structural parameters for solid-state and annealed $Na_4P_2S_6$ obtained by Rietveld refinements are available online in an additional supporting information file.

Single Crystal X-Ray Diffraction

Single crystals suitable for single-crystal X-ray diffraction were collected under a microscope in dried petroleum and mounted into sealed glass capillaries for single-crystal X-ray diffraction measurements. Diffraction data were collected at 25 °C and 227 °C on a Smart APEX-I diffractometer with a Cryostream 700Plus cooling device (Oxford Cryosystems, Oxford, United Kingdom, 80–500 K). The diffractometer (Bruker AXS, Karlsruhe, Germany) uses Mo $K\alpha$ radiation ($\lambda = 0.710\,73$ Å).

The reflection intensities were integrated with the SAINT subprogram in the Bruker Suite software package.[S5] A multi-scan absorption correction was applied using SADABS.[S6] The structure was solved by direct methods and refined by full-matrix least-squares fitting with the SHEXTL software package.[S7,S8]

Crystallographic data for β-$Na_4P_2S_6$ may be obtained from the joint CCDC/FIZ Karlsruhe online deposition service: https://www.ccdc.cam.ac.uk/structures/ by quoting the deposition number CSD-2031308.

Transmission Electron Microscopy

Powder samples of $Na_4P_2S_6$ were thoroughly ground in an agate mortar in an Argon filled glovebox and subsequently distributed onto a holey carbon/copper grid. A Philips CM 30 ST microscope (300 kV, LaB_6 cathode) was used for taking TEM images (TVIPS TemCam-F216 CMOS camera). Selected area diffraction (SAD) patterns were simulated using the JEMS software package.

Differential Scanning Calorimetry and Thermogravimetric Analysis

For Differential Scanning Calorimetry (DSC) measurements 15–25 mg of fine powdered sample were sealed in quartz ampoules (6 mm diameter, 10 to 15 mm in height) under vacuum. For improved heat flow ampoules with a flat bottom were used. DSC measurements were performed on a NETZSCH STA 449 F3 Jupiter in temperature segments of 30 °C to 300 °C. The heating and cooling rates were set to $10\,\mathrm{K\,min^{-1}}$. Due to the insulation of the furnace and its inability to actively cool, the actual temperature was cycled between 80 °C to 300 °C. Prior to measuring $Na_4P_2S_6$ samples, a temperature and DSC sensitivity calibration was performed. Thermogravimetry (TG) was measured using the same instrument as for DSC measurements. Some fine powder was filled into an open Al_2O_3-crucible and heated up to 200 °C with a heating rate of $10\,\mathrm{K\,min^{-1}}$. The data was referenced against an empty crucible to correct for buoyancy. Data evaluation was performed using the NETZSCH software package PROTEUS.

Solid-state Nuclear Magnetic Resonance Spectroscopy

All ssNMR measurements were performed on a Bruker Avance-III wide bore spectrometer in a magnetic field of 9.4 T. ^{23}Na (Larmor frequency 105.8 MHz) and ^{31}P (Larmor frequency 161.9 MHz) MAS NMR spectra were recorded in 4 mm ZrO_2 rotors using a Bruker BL4 MAS probe at a spinning speed of 10 kHz. Due to the air and moisture sensitivity of the studied materials, they were flame sealed in pyrex MAS inserts for Bruker 4 mm rotors (Wilmad Glass, product # DWGSK2576-1). Measurements on both ^{23}Na and ^{31}P were done using a simple Bloch Decay excitation scheme with a total of 512–4096 accumulations in each experiment. Long enough relaxation delays were used to provide for a complete relaxation of magnetization and ensure quantitative measurements. ^{23}Na spectra were recorded using a very short excitation pulse of $\pi/24$ to ensure homogeneous excitation of the central transitions for sites with very different quadrupolar coupling constants.[S9] The spectra were referenced to the external signals of 85% H_3PO_4 (^{31}P) and 0.1 M solution of NaCl (^{23}Na).[S10] Spectra fitting and signal integration was performed with the Dmfit software, using a Qmas$\frac{1}{2}$ model for all ^{23}Na spectra and a Gauss lineshape model for all ^{31}P spectra.[S11]

Raman Spectroscopy

Raman spectra of solid-state synthesized powder and single crystals as well as precipitated powder were recorded using a Jobin Yvon Typ V 010 LabRAM single grating spectrometer, equipped with a double super razor edge filter and a Peltier-cooled charge-coupled device camera. The resolution of the spectrometer (grating, 1800 lines/mm) was 1 cm^{-1}. The spectra were taken in a quasi-backscattering geometry using the linearly polarized 632.817 nm line of a He/Ne gas laser. The power was lower than 1 mW, to protect against local heating. The spot size was 10 µm, focused by a 50× microscope objective on to the surface of the sample. For heating experiments, the set-up is equipped with a heating microscope stage (THMS600, controlled by Linkam TMS 94). The scanning range was from 25 °C to 500 °C at a ramping rate of 5 K min^{-1} under a nitrogen atmosphere. Measurements were taken at temperatures ranging between 25 °C and 500 °C with 0.1 °C accuracy. All spectra were fitted using a Lorentz type profile for all spectral peaks form $50\,\mathrm{cm}^{-1}$ to $700\,\mathrm{cm}^{-1}$. The background was modeled to represent a broad central peak with a fixed peak center at $0\,\mathrm{cm}^{-1}$.

Bond Valence Energy Landscape Calculations

To identify possible sodium ion diffusion pathways, bond valence energy landscape (BVEL) calculations were performed using the programm 3DBVSMAPPER.[S12] The program calculates bond valence (BV) sums based on soft-BV parameters.[S13] Additionally, attraction and repulsion terms account for coulombic interactions of different ions with the tested ion and therefore convert bond valence sum maps into an energy-scaled landscape. The cutoff distance for any interaction was set to a maximum value of 8 Å. Images were created with VESTA.[S14]

Calculations

All DFT calculations were carried out with the *Vienna Ab initio Simulation Package* (VASP).[S15–S18] The PBE[S19] exchange-correlation functional with the D3[S20] dispersion correction and the PAW[S21,S22] potential were applied. For all electronic structure calculations, a convergence criterion of at least 10^{-5} eV was used. The Monkhorst-Pack[S23] k-point mesh used for Brillouin zone integration was energetically converged for all calculations while the energy-cutoff was set to 500 eV.

Nudged elastic band (NEB) calculations[S24,S25] were used to analyze the Na^+ migration in α- (0 K DFT optimized structure) and β-$\mathrm{Na_4P_2S_6}$ (experimental 200 °C structure). In these calculations we neither attempt full treatment of Na^+ disorder nor account for correlated ion motion. Scenarios with different exemplary sodium ion–vacancy orderings (belonging to three classes: Na2' $\rightleftharpoons$ Na3' intra-triple diffusion, Na2' $\rightleftharpoons$ Na3" inter-triple diffusion, and Na2' $\rightleftharpoons$ Na2" inter-triple diffusion) were chosen instead of considering partial Na^+ occupation. The results are considered to provide a qualitative understanding of the ion motion in $Na_4P_2S_6$. The pathways were chosen according to the BVEL results through tetrahedral voids (TV, Wyckoff position $8j$). Therefore, the NEB calculation was divided into two separate parts from start to TV and from TV to the final location. Simplifications were applied in order to reduce calculation time. As a first simplification, NEB calculations were, if not stated otherwise, computed in the unit cell instead of a super cell since a local migration was analyzed. Second, fixed atomic positions were used for defining start, TV, and final structures. Only the migrating Na^+ was allowed to optimize its position prior to the NEB calculation. The benchmarking of different DFT approximations, van der Waals corrections, cell sizes and increasing stages of atomic optimization can be found on page S-25 for Scenario 1. All-atom optimization reduces the E_{mig} a lot but also strongly distorts the local environment around the migrating Na^+. Overall, our calculations overestimate E_{mig} so that we only consider qualitative effects for the different examined scenarios.

Electrochemical Impedance Spectroscopy

Electrochemical impedance spectroscopy (EIS) measurements were performed using a NOVOCONTROL Technologies Alpha-A analyzer (batches ss1, ss2, p1, a1) or a NOVOCONTROL Technologies NEISYS (p2). For sample preparation fine powder of $Na_4P_2S_6$ (30–60 mg) was pressed uniaxilly at 1 GPa into pellets of 5 mm diameter. Pellets were placed between two sodium ion blocking polished steel electrodes, In-foils (batches ss1, ss2, p1, a1) or graphite foil (p2) (rhd instruments TSC Battery cell) and loaded onto a Microcell HC cell stand (rhd instruments). A spring-loaded pressure of approximately 10 MPa was applied during the measurement. The spectra were recorded in a frequency range of 3 MHz to 100 mHz and with an applied voltage of $V_{RMS} = 100\,\mathrm{mV}$. The spectra were recorded between 20 °C and 100 °C. For each prepared sample, three pellets of different cell constants (variation in pellet thickness) were measured. The average of three extracted conductivities for one sample is presented in this study. Additionally, we measured one heating and subsequent cooling cycle (1 h of equilibration between individual measurements to account for subtle differences between batches and possible hysteresis effects). Data treatment and evaluation was performed using the RHD INSTRUMENTS software package RelaxIS 3. To check data reliability, Kramers-Kronig relation tests were performed prior to fitting. Fitting the impedance spectra to equivalent circuits was done by weighting the data points proportionally. Given error bars stem from error propagation of uncertainties in pellet geometric area, pellet thickness, and applied temperature as well as errors in resistance obtained by equivalent circuit fitting. Galvanostatic polarization measurements were performed with the same two-electrode setup used for EIS measurements. Data collection was performed with a Keithley potentiostat.

Crystallographic data for α- and β-$Na_4P_2S_6$

Crystal structure of α- and β-$Na_4P_2S_6$

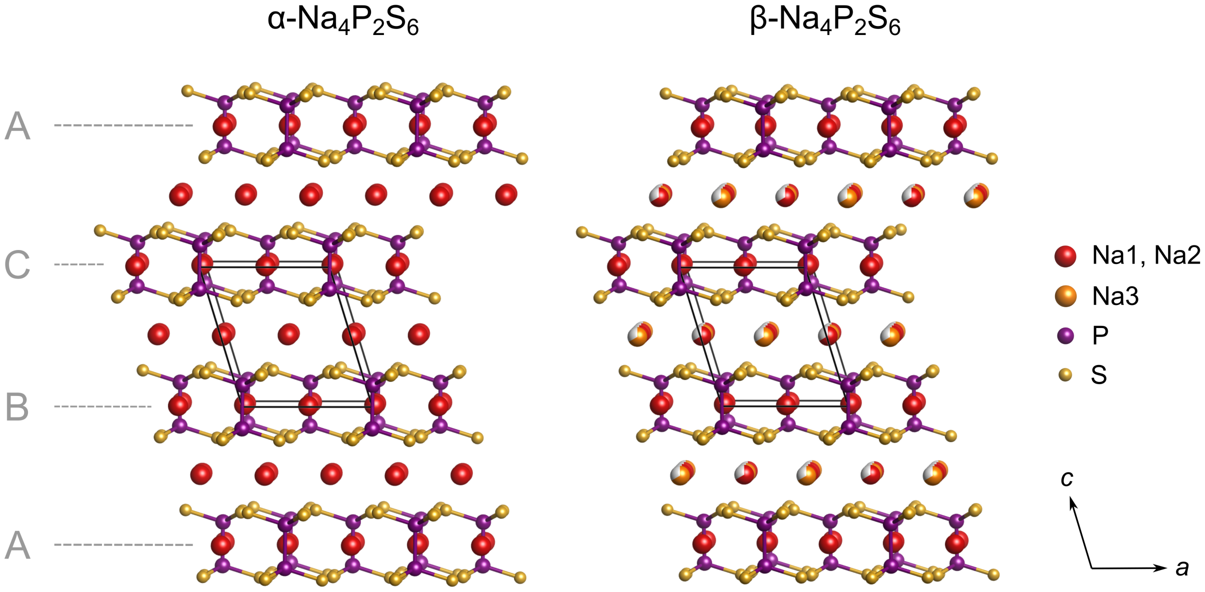

Figure S1: Layered structure of α-$Na_4P_2S_6$ at room temperature and β-$Na_4P_2S_6$ at 200 °C. The [ABC] stacking order of the $P_2S_6{}^{4-}$ is indicated by capital Latin letters.

Solid-state synthesis

Table S1: Crystallographic data and refinement details. Statistical errors as obtained from the Rietveld refinements are given in parentheses.

	α-$Na_4P_2S_6$	β-$Na_4P_2S_6$	β-$Na_4P_2S_6$
Temperature ϑ (°C)	20	200	500
Formula weight M ($\mathrm{g\,mol^{-1}}$)	346.3	346.3	346.3
Crystal system	monoclinic	monoclinic	monoclinic
Space group	$C2/m$ (no. 12)	$C2/m$ (no. 12)	$C2/m$ (no. 12)
Lattice parameter a (Å)	6.7358(2)	6.6595(2)	6.7094(3)
Lattice parameter b (Å)	11.1998(3)	11.4256(4)	11.5522(6)
Lattice parameter c (Å)	7.5309(2)	7.6523(3)	7.7786(1)
Monoclinic angle β (°)	107.000(2)	107.093(3)	107.504(3)
Volume V ($\mathrm{Å^3}$)	543.31(3)	556.53(3)	575.58(5)
Formula units Z	2	2	2
Crystallographic density ρ ($\mathrm{g\,cm^{-3}}$)	2.12	2.07	2.00
X-ray radiation	Mo $K\alpha_1$	Mo $K\alpha_1$	Mo $K\alpha_1$
2θ range (°)	2.000–61.835	2.000–61.835	4.000–35.905
No. of refined parameters	55	55	55
No. of restraints/constraints	0/3	0/3	0/3
R_p, R_wp (%)	4.8/6.0	4.1/5.3	5.7/7.1
R_Bragg, R_F (%)	7.9/5.0	7.3/5.1	8.7/6.5

Table S2: Atomic positions and displacement parameters of α-$Na_4P_2S_6$ at 20 °C. Statistical errors as obtained from the Rietveld refinement are given in parentheses.

Atom	Wyckoff position	x	y	z	U_iso ($\mathrm{Å^2}$)	Occupancy
Na1	$4g$	0.5	0.1625(6)	0	0.031(1)	1
Na2	$4h$	0.5	0.3177(4)	0.5	0.031(1)	0.981(4)
Na3	$2d$	0	0.5	0.5	0.031(1)	2(1–Occ(Na2))
P1	$4i$	0.5569(5)	0.5	0.1507(4)	0.019(1)	1
S1	$4i$	0.2916(5)	0.5	0.2423(4)	0.019(1)	1
S2	$8j$	0.7244(4)	0.3489(2)	0.2325(3)	0.0220(9)	1

Table S3: Atomic positions and displacement parameters of β-$Na_4P_2S_6$ at 200 °C. Statistical errors as obtained from the Rietveld refinement are given in parentheses.

Atom	site	x	y	z	U_{iso} (Å^2)	Occupancy
Na1	$4g$	0.5	0.1625(5)	0	0.066(2)	1
Na2	$4h$	0.5	0.3218(7)	0.5	0.066(2)	0.679(3)
Na3	$2d$	0	0.5	0.5	0.066(2)	2(1–Occ(Na2))
P1	$4i$	0.5504(6)	0.5	0.1498(4)	0.026(1)	1
S1	$4i$	0.2836(7)	0.5	0.2341(4)	0.045(2)	1
S2	$8j$	0.7251(5)	0.3519(2)	0.2343(3)	0.040(1)	1

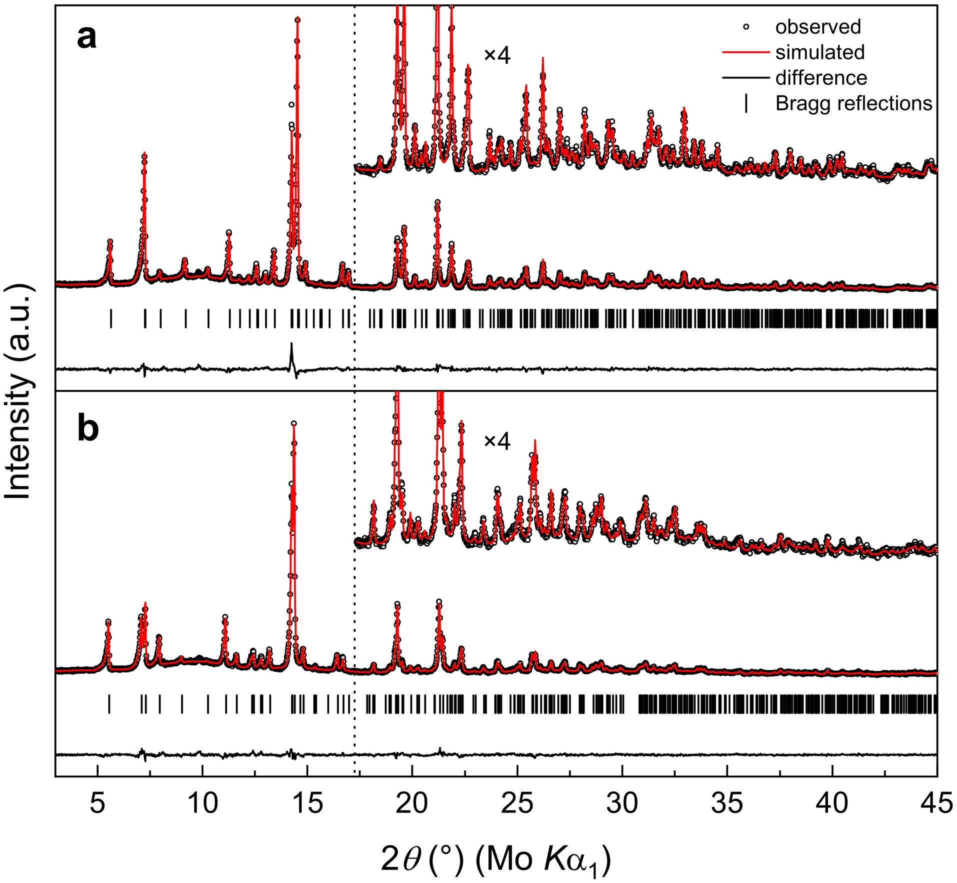

Figure S2: Rietveld refinement of **a** α-$Na_4P_2S_6$ at 20 °C and **b** β-$Na_4P_2S_6$ at 200 °C.

Table S4: Atomic positions and displacement parameters of β-$Na_4P_2S_6$ at 500 °C. Statistical errors as obtained from the Rietveld refinement are given in parentheses.

Atom	site	x	y	z	U_{iso} (Å^2)	Occupancy
Na1	$4g$	0.5	0.1615(5)	0	0.123(3)	1
Na2	$4h$	0.5	0.3333(7)	0.5	0.123(3)	0.654(5)
Na3	$2d$	0	0.5	0.5	0.123(3)	2(1–Occ(Na2))
P1	$4i$	0.5488(8)	0.5	0.1440(6)	0.037(2)	1
S1	$4i$	0.2883(7)	0.5	0.2364(6)	0.094(3)	1
S2	$8j$	0.7265(7)	0.3525(5)	0.2369(6)	0.088(2)	1

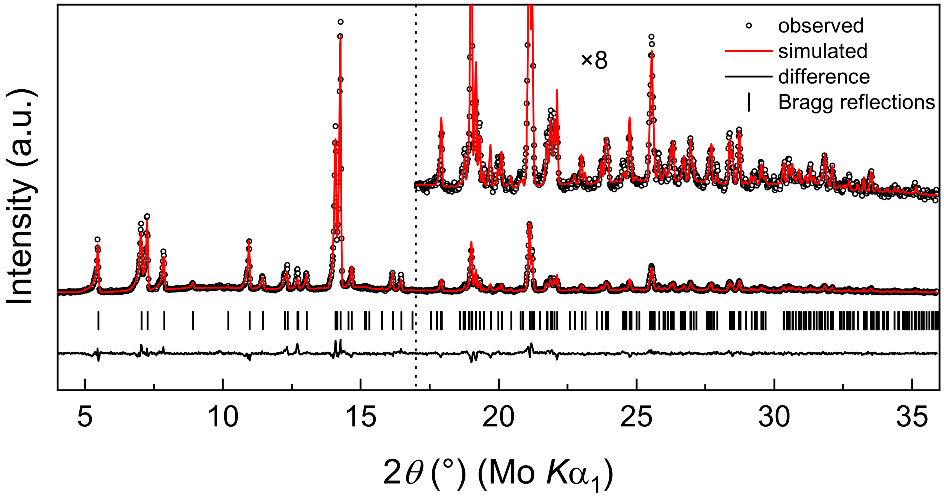

Figure S3: Rietveld refinement of β-$Na_4P_2S_6$ at 500 °C.

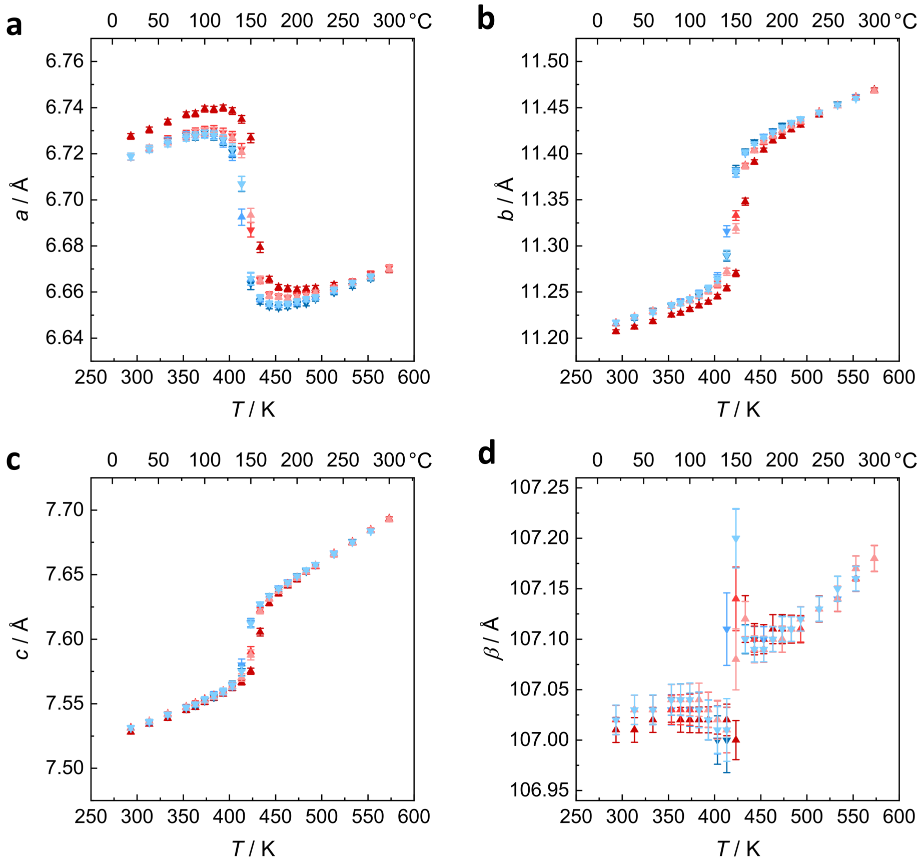

Figure S4: Results of the Rietveld refinements for the α–β phase transition in solid-state $Na_4P_2S_6$ upon heating and cooling. (**a**–**d**) Lattice parameters a, b, c and monoclinic angle β.

Annealed solution-synthesized $Na_4P_2S_6$

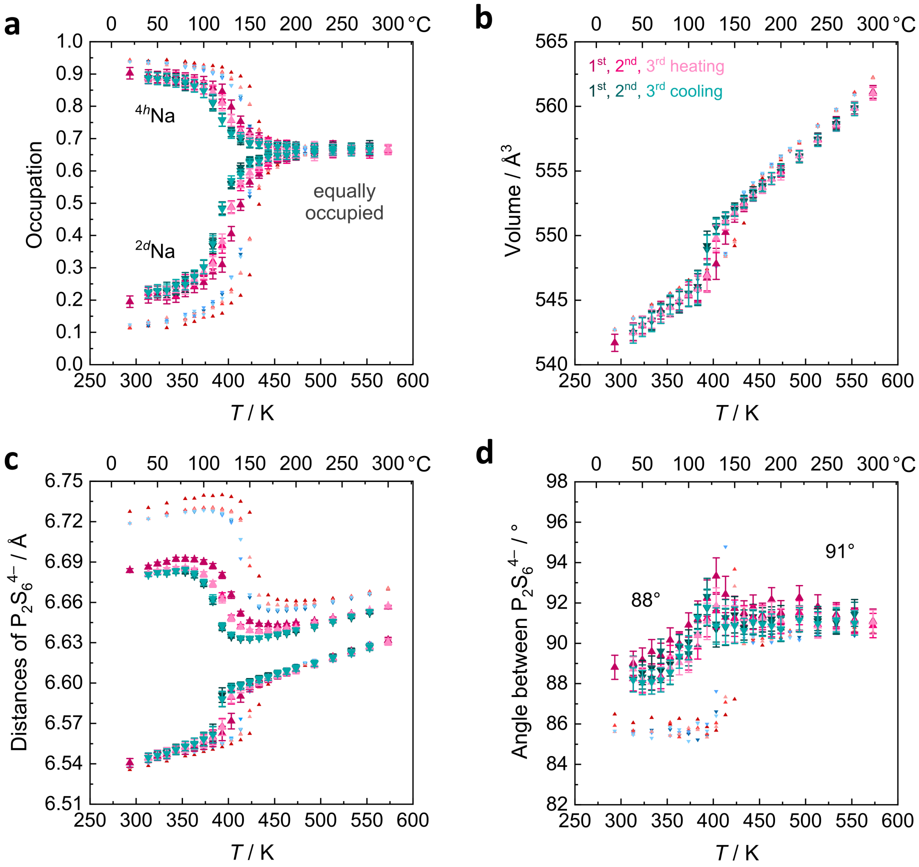

Figure S5: Results of the Rietveld refinements for the α–β phase transition in annealed $Na_4P_2S_6$ (bold data markers) upon heating (pink data points) and cooling (teal data points) for the first three cycles (color code from dark to light with increasing cycle number). Small data markers are taken from the solid-state synthesized $Na_4P_2S_6$ for comparison. **a** Occupation of the sodium positions Na2 and Na3 between the $P_2S_6{}^{4-}$ layers. **b** Volume change with temperature. **c** Distances of the $P_2S_6{}^{4-}$ anions as a measure for the hexagonality of the layer. **d** Tilting of neighboring $P_2S_6{}^{4-}$ anions in a direction expressed as the P–P–P_{neighbor} angle.

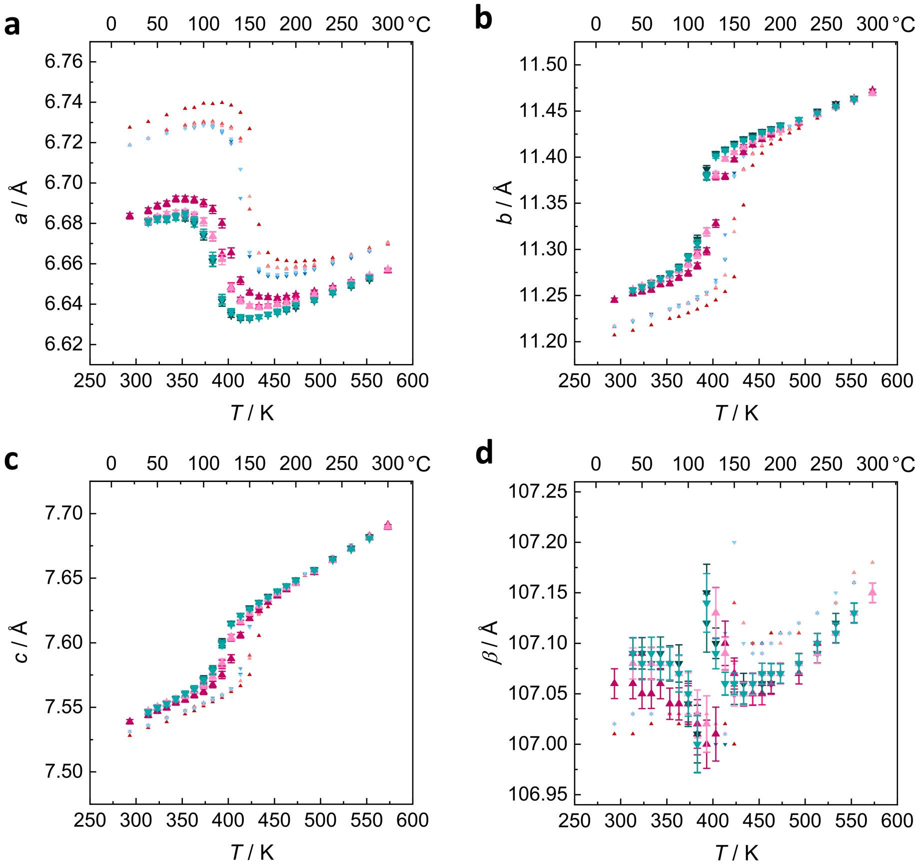

Figure S6: Results of the Rietveld refinements for the α–β phase transition in annealed $Na_4P_2S_6$ upon heating and cooling (bold data markers). Small data markers are taken from the solid-state synthesized $Na_4P_2S_6$ for comparison. (**a**–**d**) Lattice parameters a, b, c and monoclinic angle β.

Single crystal

Table S5: Crystallographic data as obtained from single-crystal X-ray diffraction (Mo $K\alpha$) measured **a** at 25 °C, **b** subsequently at 227 °C, and **c** again at 25 °C.

	a α-$Na_4P_2S_6$	**b** β-$Na_4P_2S_6$	**c** α-$Na_4P_2S_6$
Temperature ϑ (K)	298	500	298
Formula weight M ($\mathrm{g\,mol^{-1}}$)	346.3	346.3	346.3
Crystal system	monoclinic	monoclinic	monoclinic
Space group	$C2/m$ (no. 12)	$C2/m$ (no. 12)	$C2/m$ (no. 12)
Lattice parameter a (Å)	6.761(1)	6.671(3)	6.760(1)
Lattice parameter b (Å)	11.233(2)	11.450(5)	11.234(2)
Lattice parameter c (Å)	7.549(2)	7.663(4)	7.550(2)
Monoclinic angle β (°)	107.034(3)	107.107(7)	107.034(3)
Volume V ($\mathrm{\AA^3}$)	548.2(2)	559.5(4)	548.2(2)
Formula units Z	2	2	2
Crystallographic density ρ ($\mathrm{g\,cm^{-3}}$)	2.10	2.06	2.10
2θ range (°)	2.822–35.353	2.781–35.341	2.822–35.353
Index range	$-10 \leq h \leq 10$	$-10 \leq h \leq 10$	$-10 \leq h \leq 10$
	$-17 \leq k \leq 17$	$-18 \leq k \leq 18$	$-17 \leq k \leq 17$
	$-11 \leq l \leq 12$	$-12 \leq l \leq 12$	$-12 \leq l \leq 11$
Total reflections	4141	3838	4257
Unique reflections	1224	1246	1226
Parameters	32	38	32
$R_1(\geq 2\sigma)$ (%)	2.9	4.6	3.1
wR_2 ($\geq 2\sigma$) (%)	7.7	10.9	8.6
GooF	1.1	1.2	1.1

Table S6: Atomic coordinates and equivalent isotropic displacement factors of **a** α-$Na_4P_2S_6$ at 298 K.

Atom	site	x	y	z	U_{eq} ($\mathrm{\AA}^2$)	Occupancy
Na1	4g	0.5	0.16203(9)	0	0.0267(2)	1
Na2	4h	0.5	0.3149(1)	0.5	0.0305(2)	1
P1	4i	0.55377(8)	0.5	0.15629(7)	0.0146(1)	1
S1	4i	0.29560(8)	0.5	0.24190(7)	0.0197(1)	1
S2	8j	0.72262(6)	0.34949(4)	0.23026(5)	0.0219(1)	1

Table S7: Atomic coordinates and equivalent isotropic displacement factors of **b** β-$Na_4P_2S_6$ at 500 K.

Atom	site	x	y	z	U_{eq} ($\mathrm{\AA}^2$)	Occupancy
Na1	4g	0.5	0.1659(2)	0	0.0495(4)	1
Na2	4h	0.5	0.3199(4)	0.5	0.077(1)	0.656(2)
Na3	2d	0	0.5	0.5	0.109(2)	2(1–Occ(Na2))
P1	4i	0.5502(1)	0.5	0.1539(1)	0.0260(2)	1
S1	4i	0.2860(2)	0.5	0.2311(1)	0.0412(2)	1
S2	8j	0.7229(1)	0.35324(6)	0.2320(1)	0.0397(2)	1

Table S8: Atomic coordinates and equivalent isotropic displacement factors of **c** α-$Na_4P_2S_6$ at 298 K after heating to 500 K.

Atom	site	x	y	z	U_{eq} ($\mathrm{\AA}^2$)	Occupancy
Na1	4g	0.5	0.1620(1)	0	0.0267(2)	1
Na2	4h	0.5	0.3149(1)	0.5	0.0305(3)	1
P1	4i	0.55377(9)	0.5	0.15627(8)	0.0147(1)	1
S1	4i	0.29560(9)	0.5	0.24192(9)	0.0197(1)	1
S2	8j	0.72256(7)	0.34946(4)	0.23024(5)	0.0219(1)	1

Differential scanning calorimetry

After performing DSC on the three $Na_4P_2S_6$ samples we opened the sealed quartz glass ampoules to record PXRD patterns. A comparison of before and after DSC powder diffraction patterns is given in Figure S7. Although, the patterns of the DSC treated samples (four-times cycling up to 300 °C) show good agreement to the patterns recorded prior to the DSC, some new reflections mainly around 10° 2θ (Mo $K\alpha_1$) arise in the precipitated $Na_4P_2S_6$ (see Figure S7b). We account this to some degree of annealing, since the position of the new reflections is comparable to reflections found in both solid-state and annealed $Na_4P_2S_6$. Cycling the temperature for a few times up to 300 °C over the course of a few hours might have a similar impact on "healing" the β-like precipitated sample as annealing it at 500 °C for a shorter time. Since the ampoules did not show any indication of reaction with the sample, like discoloration or opacification, we exclude degradation of the powder during DSC.

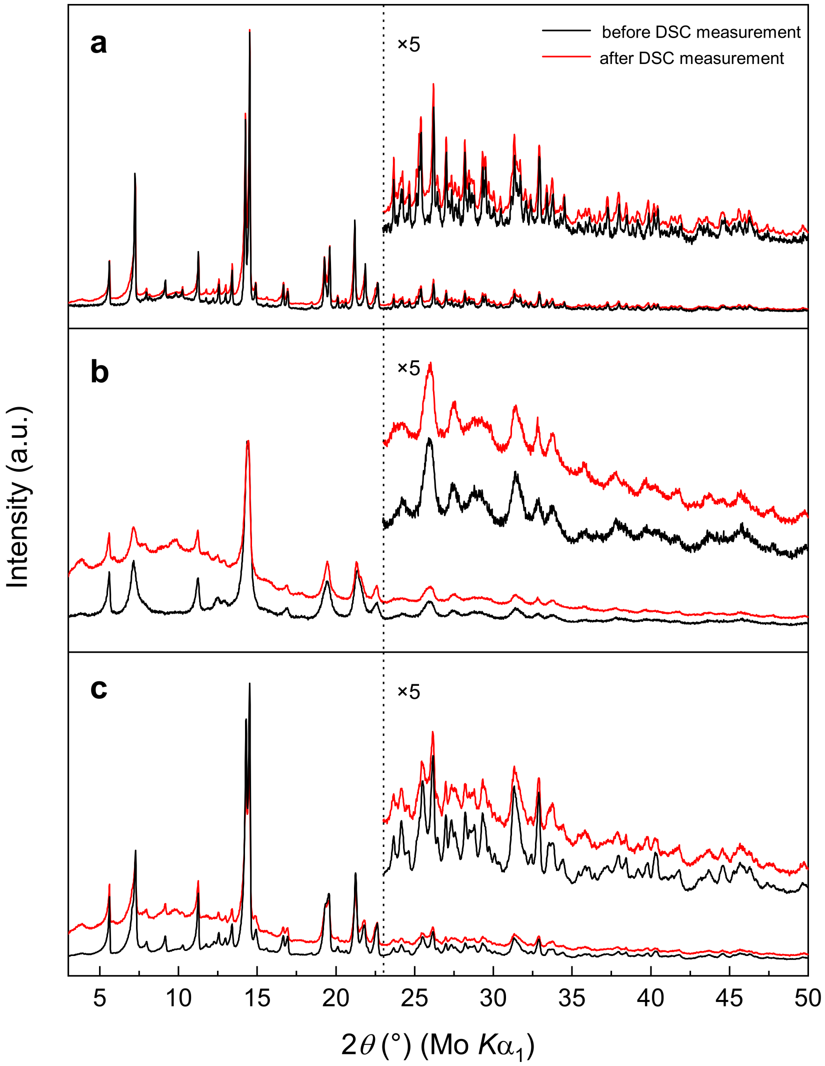

Figure S7: Room temperature PXRD patterns of **a** solid-state, **b** precipitated, and **c** annealed $Na_4P_2S_6$ before and after DSC measurements up to 300 °C.

Thermogravimetric analysis

Precipitated $Na_4P_2S_6$ was checked for residual water after drying the hydrate precursor in a Büchi furnace (*cf.* Experimental Section). A thermogravietric diagram is shown in Figure S8. The dried compound still holds some residual water, however, the amount is small enough to consider this material as dry. Assuming the observed weight loss to be crystal water, a sum formula is calculated to $Na_4P_2S_6 \cdot 0.004\,H_2O$. Since some degree of re-hydration in air cannot be rules out during the transfer into the instrument, we are confident that the dehydration procedure yields virtually crystal water free $Na_4P_2S_6$.

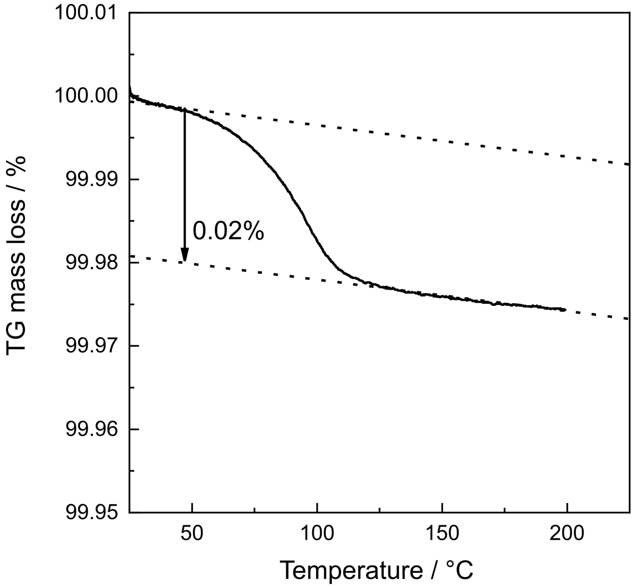

Figure S8: Thermogram of precipitated $Na_4P_2S_6$.

Raman spectroscopy

The molecular anion ${P_2S_6}^{4-}$ can exist in two different point group symmetries, depending on the chemical surrounding. The more symmetrical configuration D_{3d} resembles the symmetry of an ethane molecule, composed of two trigonal pyramids that are connected *via* a central homonuclear bond (C–C or P–P). This symmetry is for example found in $Mg_2P_2S_6$, $(NH_4)_4P_2S_6$, $Na_4P_2S_6 \cdot 6\,H_2O$, and $Li_4P_2S_6$.[S26,S27] An analysis of the vibrational modes of a molecule of D_{3d} gives:

$$\Gamma_{vib}(D_{3d}) = 3A_{1g}(R) + 1A_{1u}(ia) + 2A_{2u}(IR) + 3E_g(R) + 3E_u(IR),$$

with R being Raman active modes, IR being infrared active modes, and ia being inactive modes. Therefore six Raman active modes should be present for an ${P_2S_6}^{4-}$ of ethane-like symmetry.

By slightly elongating or shortening one P–S bond and changing the corresponding S–P–S angle the ${P_2S_6}^{4-}$ anion adapts a less symmetrical C_{2h} point symmetry. Anions of this kind are found in $Ca_2P_2S_6$, $Sr_2P_2S_6$, $Ba_2P_2S_6$, and $Sn_2P_2S_6$.[S26,S28] According to the analysis the vibrational modes for a molecule of this symmetry,

$$\Gamma_{vib}(C_{2h}) = 6A_g(R) + 4A_u(IR) + 3B_g(R) + 5B_u(IR),$$

nine Raman active modes are expected. A visualization of the ${P_2S_6}^{4-}$ anion in α- (C_{2h}) and β- (D_{3d}) $Na_4P_2S_6$ is shown in Figure S9.

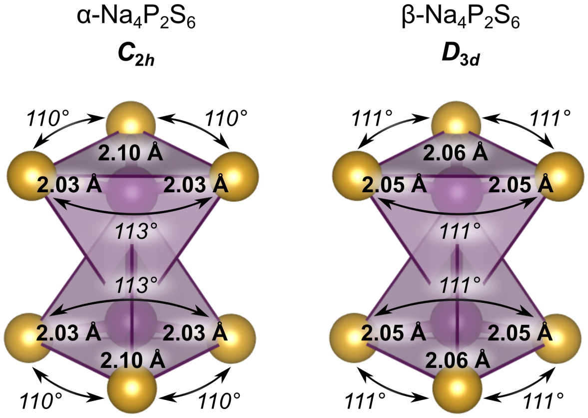

Figure S9: $P_2S_6{}^{4-}$ anion in α- and β-$Na_4P_2S_6$ at 20 °C and 200 °C with C_{2h} and D_{3d} symmetry, respectively.

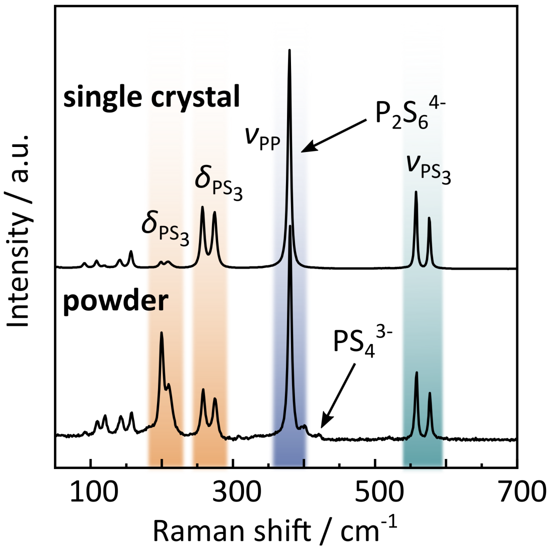

Figure S10: Room temperature Raman spectra of solid-state synthesized $Na_4P_2S_6$ powder with a more pronounced deformation mode around 200 cm^{-1} compared to the single crystal.

Table S9: Vibrational frequencies of solid-state synthesized $Na_4P_2S_6$ in cm^{-1}.

Asgmt	Mode	Temperature / °C								Asgmt	Mode
C_{2h}		25	100	150	200	250	300	400	500	D_{3d}	
presumably		91 vw									
lattice		108 w	107 w	106 w	99 vw	102 vw	100 vw	100 vw	97 vw	lattice vib.	
vibrations		119 w	118 vw	117 vw	117 sh						
δ_{PS_3}		141 vw	140 vw	140 vw	142 vw	140 w	137 w	137 w	137 w	δ_{PS_3}	
		156 vw	155 vw	155 vw							
δ_{PS_3}		198 vw	204 vw	202 vw	194 vw	193 vw	192 vw	189 vw	187 vw	δ_{PS_3}	A_{1g} or E_g
δ_{PS_3}		208 vw									
δ_{PS_3}	A_g	257 s	257 s	257 m	264 s	264 s	263 s	262 s	261 s	δ_{PS_3}	E_g
δ_{PS_3}	B_g	274 w	273 w	273 w							
ν_{PP}	A_g	379 vs	378 vs	378 vs	376 vs	375 vs	375 vs	373 vs	371 vs	ν_{PP}	A_{1g}
ν_{PS_3}	A_g	557 s	556 s	554 s	550 s	549 s	548 s	545 s	542 s	ν_{PS_3}	A_{1g}
ν_{PS_3}	A_g	con	con	con	569 sh	567 sh	566 sh	560 sh	554 sh	ν_{PS_3}	E_g
ν_{PS_3}	B_g	576 m	575 m	574 m							

ν: stretching mode, δ: bending mode, w = weak, m = medium, s = strong, v = very, sh = shoulder,

con = convoluted with ν_{PS_3} (A_g) mode at 556 cm^{-1}.

Cationic and anionic sublattice

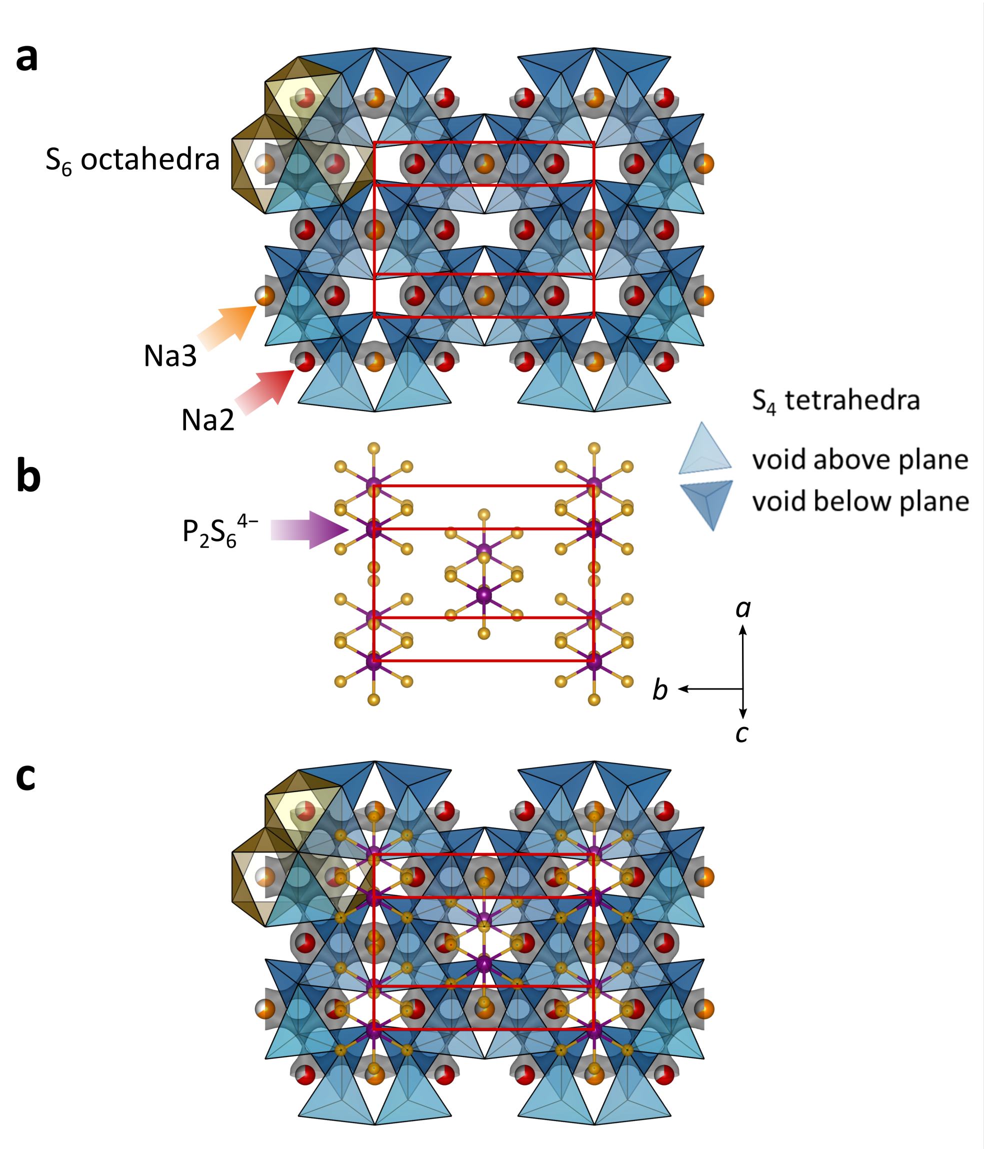

Figure S11: **a** Na2/Na3 cation and **b** $P_2S_6{}^{4-}$ anion order in β-$Na_4P_2S_6$. **c** Superimposed images of **a** and **b**.

DFT calculations

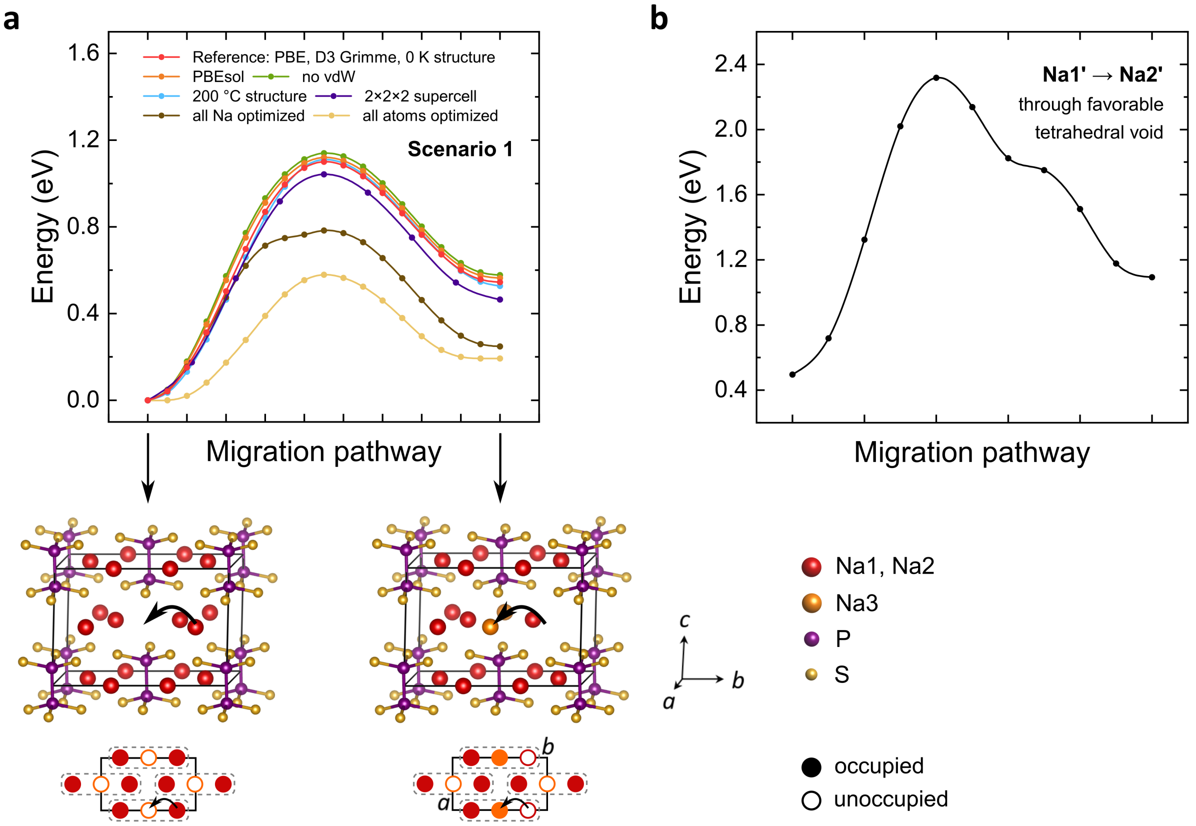

Figure S12: Energy curves for Na^+ migration in $Na_4P_2S_6$ from NEB calculations. **a** Comparison of different DFT inputs for Scenario 1 to the reference used in the main text (PBE approximation, D3 Grimme van der Waals correction, DFT-optimized structure (0 K), unit cell, fixed atom positions). PBEsol: PBEsol approximation. no vdW: without D3 correction. 200 °C: experimental 200 °C structure. 2 × 2 × 2 supercell. All Na/all atoms optimized in the NEB calculation. **b** Migration of Na1 through a favorable tetrahedral void to the Na2/Na3 layer with an $E_{\mathrm{mig}} = 1.82\,\mathrm{eV}$.

Impedance Spectroscopy and DC Polarization

In this section the fitting process of the measured impedance spectra and the DC polarization measurement is discussed.

Impedance spectroscopy

Typically, impedance spectra of pure ion conductors are composed of a semicircle at high frequencies, described as a parallel arrangement of a resistance R and a constant phase element CPE, followed by a polarization spike at low frequencies, modeled as a second CPE in series of the parallel (R)(CPE1) circuit. For this study, some spectra were fitted using an additional capacitor C parallel to the (R)(CPE1)–CPE2 circuit, to account for parasitic stray capacitance.[S29] The stray capacitance was found to be on the order of a few pF for all measured temperatures. Constant phase elements are often used to describe a non ideal behavior entailing a dispersion of relaxation times, often stemming from microscopically imperfect contacts at the sample–electrode contact or a distribution in material properties and thus a non-uniform current through the sample.[S30] To extract an effective capacitance (in units of F) from a CPE parallel to a resistance R, the Brug formula $C_{Brug} = Q^{\frac{1}{\alpha}} R^{(\frac{1}{\alpha}-1)}$ is widely used, with Q being the CPE's numerical value of admittance, α being the element's exponential factor, and R being the resistivity in units of Ω.[S31]

Ionic conductivties were calculated by $\sigma_{ion} = \frac{1}{R}\frac{d}{A}$, with R being the resistivity, d being the sample thickness, and A being the geometrical electrode area.

Electronic conductivity

The electronic conductivity σ_{eon} of a material with an ionic conductivity σ_{eon} and a total conductivity of σ can be determined by measuring the DC galvanostatic polarization in an ion blocking configuration. Cold-pressed pellets of ss2 and p1 $Na_4P_2S_6$ with a thickness of L were sandwiched between two stainless steel electrodes. A constant current I of 1 or 10 nA, depending on the sample, was applied for 2400 s. The polarization curves of ss2 and p1 samples are shown in Figure S13. The transient time τ^δ (represented as a grey box) was too short to reach a steady state condition (zero slope) but was sufficiently long to reach a region of linear slope (potential U as a function of the square root of time t). The electronic contribution can be estimated by solving the following linear equation[S32] for σ_{eon}:

$$U - U_{GB} = \frac{IL}{\sigma} + \frac{\sigma_{ion}}{\sigma}\frac{IL}{\sigma_{eon}}\frac{4}{\pi^{\frac{3}{2}}}\sqrt{\frac{t}{\tau^\delta}}$$

This equation describes the evolution of the potential under an applied current for the characteristic semi-finite chemical diffusion time τ^δ. For practical measurements τ^δ is the time of applied current (here 2400 s). For solving the equation, we made the assumption of $\sigma_{eon} \ll \sigma_{ion}$, hence $\sigma \approx \sigma_{ion}$. Furthermore we expect no significant grain boundary contribution (negligible U_{GB}) since the extracted capacities on the order of 10 pF/cm^2 suggest a bulk rather than a grain boundary limited process. Recently Dawson *et al.* have calculated that for Na_3PS_4 no significant grain-boundary resistance is present in poly-crystalline samples,[S33] which is in good agreement with the experimental findings of Krauskopf *et al.*.[S34] We therefore suspect a similar behaviour for $Na_4P_2S_6$.

With these assumptions made we estimate the electronic conductivity of p1 and ss2 $Na_4P_2S_6$ samples to be $1.4 \cdot 10^{-10}\,\mathrm{S\,cm^{-1}}$ and $2.6 \cdot 10^{-9}\,\mathrm{S\,cm^{-1}}$, respectively. The transference number $t(\mathrm{Na}^+)$, describing the ratio of sodium ion conductivity to total (ionic and electronic) conductivity, is ≤ 0.99. Hence, $Na_4P_2S_6$ can be described as a nearly pure sodium ion conductor.

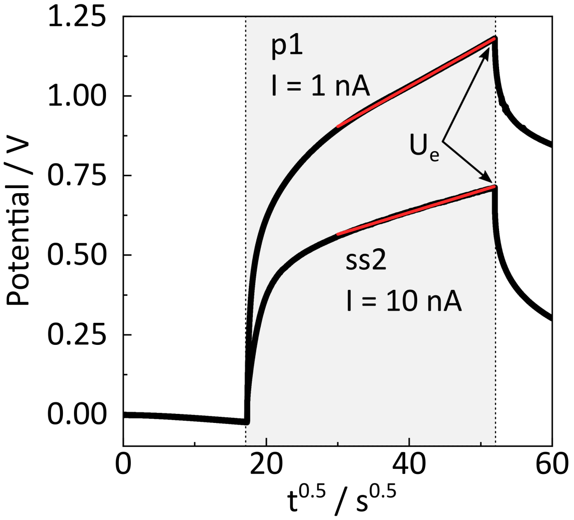

Figure S13: DC galvanostatic polarization measurements on ss2 and p1 samples of $Na_4P_2S_6$ at room temperature. Pressed pellets were contacted with steel electrodes in an ion blocking configuration.

References

(S1) Kuhn, A.; Eger, R.; Nuss, J.; Lotsch, B. V. Synthesis and Structural Characterization of the Alkali Thiophosphates $Na_2P_2S_6$, $Na_4P_2S_6$, $K_4P_2S_6$, and $Rb_4P_2S_6$. *Z. Anorg. Allg. Chem.* **2014**, *640*, 689–692.

(S2) Fincher, T.; LeBret, G.; Cleary, D. A. Single-Crystal Structure Determination of $Na_4P_2S_6 \cdot 6\,H_2O$. *J. Solid State Chem.* **1998**, *141*, 274–281.

(S3) Petříček, V.; Dušek, M.; Palatinus, L. Crystallographic Computing System JANA2006: General features. *Z. Kristallogr.* **2014**, *229*, 345–352.

(S4) Rietveld, H. M. A profile refinement method for nuclear and magnetic structures. *J. Appl. Cryst.* **1969**, *2*, 65–71.

(S5) Bruker Suite, Version 2019.1. Bruker AXS Inc., Madison, WI, USA. 2019.

(S6) Krause, L.; Herbst-Irmer, R.; Sheldrick, G. M.; Stalke, D. Comparison of silver and molybdenum microfocus X-ray sources for single-crystal structure determination. *J. Appl. Cryst.* **2015**, *48*, 3–10.

(S7) Sheldrick, G. M. A short history of *SHELX*. *Acta Crystallogr. Sect. A: Found. Crystallogr.* **2008**, *64*, 112–122.

(S8) Sheldrick, G. M. Crystal structure refinement with *SHELXL*. *Acta Crystallogr., Sect. C: Struct. Chem.* **2015**, *71*, 3–8.

(S9) Freude, D.; Haase, J. Quadrupole Effects in Solid-state NMR. website, 2013–2019; www.quad-nmr.de.

(S10) Harris, R. K.; Becker, E. D.; de Menezes, S. M. C.; Goodfellow, R.; Granger, P. NMR Nomenclature: Nuclear Spin Properties and Conventions for Chemical Shifts. IUPAC Recommendations 2001. *Solid State Nucl. Magn. Reson.* **2002**, *22(4)*, 458–483.

(S11) Massiot, D.; Fayon, F.; Capron, M.; King, I.; Le Calvé, S.; Alonso, B.; Durand, J.-O.; Bujoli, B.; Gan, Z.; Hoatson, G. Modelling one- and two-dimensional solid-state NMR spectra. *Magn. Reson. Chem.* **2002**, *40*, 70–76.

(S12) Sale, M.; Avdeev, M. *3DBVSMAPPER*: a program for automatically generating bond-valence sum landscapes. *J. Appl. Cryst.* **2012**, *45*, 1054–1056.

(S13) Adams, S.; Rao, R. P. High power lithium ion battery materials by computational design. *Phys. Status Solidi A* **2011**, *208*, 1746–1753.

(S14) Momma, K.; Izumi, F. *VESTA3* for three-dimensional visualization of crystal, volumetric and morphology data. *J. Appl. Cryst.* **2011**, *44*, 1272–1276.

(S15) Kresse, G.; Hafner, J. Ab initio molecular dynamics for liquid metals. *Phys. Rev. B* **1993**, *47*, 558–561.

(S16) Kresse, G.; Hafner, J. Ab initio molecular-dynamics simulation of the liquid-metal–amorphous-semiconductor transition in germanium. *Phys. Rev. B* **1994**, *49*, 14251–14269.

(S17) Kresse, G.; Furthmüller, J. Efficiency of ab-initio total energy calculations for metals and semiconductors using a plane-wave basis set. *Comput. Mater. Sci.* **1996**, *6*, 15–50.

(S18) Kresse, G.; Furthmüller, J. Efficient iterative schemes for ab initio total-energy calculations using a plane-wave basis set. *Phys. Rev. B* **1996**, *54*, 11169–11186.

(S19) Perdew, J. P.; Burke, K.; Ernzerhof, M. Generalized Gradient Approximation Made Simple. *Phys. Rev. Lett.* **1996**, *77*, 3865–3868.

(S20) Grimme, S.; Antony, J.; Ehrlich, S.; Krieg, H. A consistent and accurate ab initio parametrization of density functional dispersion correction (DFT-D) for the 94 elements H-Pu. *J. Chem. Phys.* **2010**, *132*, 154104.

(S21) Blöchl, P. E. Projector augmented-wave method. *Phys. Rev. B* **1994**, *50*, 17953–17979.

(S22) Kresse, G.; Joubert, D. From ultrasoft pseudopotentials to the projector augmented-wave method. *Phys. Rev. B* **1999**, *59*, 1758–1775.

(S23) Monkhorst, H. J.; Pack, J. D. Special points for Brillouin-zone integrations. *Phys. Rev. B* **1976**, *13*, 5188–5192.

(S24) Mills, G.; Jónsson, H.; Schenter, G. K. Reversible work transition state theory: application to dissociative adsorption of hydrogen. *Surf. Sci.* **1995**, *324*, 305–337.

(S25) Jónsson, H.; Mills, G.; Jacobsen, K. W. Nudged elastic band method for finding minimum energy paths of transitions, in Classical and Quantum Dynamics in Condensed Phase Simulations, ed. B. J. Berne, G. Ciccotti and D. F. Coker (World Scientific, 1998).

(S26) Pätzmann, U.; Brockner, W. Raman-Spektren der Hexathiohypodiphosphate des NH_4, Mg, Ca, Sr und Ba. *Z. Naturforsch. A* **1987**, *42*, 593–596.

(S27) Dietrich, C.; Sadowski, M.; Sicolo, S.; Weber, D. A.; Sedlmaier, S. J.; Weldert, K. S.; Indris, S.; Albe, K.; Janek, J.; Zeier, W. G. Local Structural Investigations, Defect Formation, and Ionic Conductivity of the Lithium Ionic Conductor $Li_4P_2S_6$. *Chem. Mater.* **2016**, *28*, 8764–8773.

(S28) Becker, R.; Brockner, W.; Wibbelmann, C. Schwingungsspektren von $Sn_2P_2S_6$ / Vibrational Spectra of $Sn_2P_2S_6$. *Z. Naturforsch. A* **1983**, *38*, 555–558.

(S29) Kuhn, A.; Duppel, V.; Lotsch, B. V. Tetragonal $Li_{10}GeP_2S_{12}$ and Li_7GePS_8 – exploring the Li ion dynamics in LGPS Li electrolytes. *Energy Environ. Sci.* **2013**, *6*, 3548–3552.

(S30) Barsoukov, E.; Macdonald, J. R. *Impedance Spectroscopy Theory, Experiment, and Applications*; JohnWiley & Sons, Inc.: Hoboken, NJ, 2005; p 15.

(S31) Brug, G.; van den Eeden, A.; Sluyters-Rehbach, M.; Sluyters, J. The analysis of electrode impedances complicated by the presence of a constant phase element. *J. Electroanal. Chem. Interf. Electrochem.* **1984**, *176*, 275–295.

(S32) Maier, J. *Physical Chemistry of Ionic Materials*; John Wiley & Sons, Ltd., 2005; Chapter 7, pp 399–499.

(S33) Dawson, J. A.; Canepa, P.; Clarke, M. J.; Famprikis, T.; Ghosh, D.; Islam, M. S. Toward Understanding the Different Influences of Grain Boundaries on Ion Transport in Sulfide and Oxide Solid Electrolytes. *Chem. Mater.* **2019**, *31*, 5296–5304.

(S34) Krauskopf, T.; Culver, S. P.; Zeier, W. G. Local Tetragonal Structure of the Cubic Superionic Conductor Na_3PS_4. *Inorg. Chem.* **2018**, *57*, 4739–4744.